



Defect-driven electroless deposition and activation of platinum sites on ZnIn₂S₄ nanosheets for accelerated kinetics of photocatalytic hydrogen production

Yanhui Su^{a,b}, Zhihe Wei^{a,b}, Yuebin Lian^c, Qiaoqiao Mu^a, Weiyei Pan^{a,b}, Daqi Song^{a,b}, Yongze Qin^a, Wei Hua^a, Jian Cheng^{a,b}, Zhao Deng^a, Yang Peng^{a,b,*}

^a Soochow Institute of Energy and Material Innovations, College of Energy, Jiangsu Key Laboratory for Advanced Carbon Materials and Wearable Energy Technologies, Soochow University, Suzhou 215006, China

^b Jiangsu Key Laboratory of Advanced Negative Carbon Technologies, Soochow University, Suzhou 215123, Jiangsu, China

^c School of Photoelectric Engineering, Changzhou Institute of Technology, Changzhou 213032, China

ARTICLE INFO

Keywords:

Photocatalysis
ZnIn₂S₄ Nanosheets
Defect sites
Pt atoms/clusters

ABSTRACT

The role of defects introduced into photocatalysts has been controversial, as some claim they serve as electron-trapping sites for improving the photogenerated charge separation, while others argue they act as exciton recombination centers to shorten the lifetime and mean free path of photocarriers. In the current study, we show the defect sites introduced into Zinc indium sulfide (ZIS) function as a double-bladed sword: on one hand, they act as recombination centers to impede photogenerated electron-hole separation in bulk ZIS; on the other hand, they drive electroless deposition and activation of the Pt co-catalyst through strong electronic coupling and thereby drastically enhance photocatalytic hydrogen production. As such, the defect-rich ZIS with a moderate Pt loading manifests the best hydrogen evolution rate of 15.56 mmol h⁻¹ g⁻¹ with a superb Pt-based TOF of 2334 h⁻¹, apart from a high TON of 99610 in 92 h, which are among the best reported in literature for chalcogenide-based photocatalysts. Comprehensive microscopic, spectroscopic and photoelectrochemical characterizations unveil that the intimate coupling between the ZIS vacancy sites and deposited Pt atoms/clusters not only promotes photoexcited electron-hole separation, but also modulates local charge polarization to leverage the intrinsic activity of the co-catalyst.

1. Introduction

Colloidal photocatalytic hydrogen evolution probably represents the most economic way to mass-produce hydrogen through the direct exploitation of solar energy [1,2]. At the core of this green energy technology is the development of highly efficient photocatalysts with three intrinsic attributes key to the photocatalytic process, namely, the high efficacy of light absorption, the efficient separation of photocarriers, and the high turnover rate at the active sites [3,4]. Besides, the high photochemical stability is also paramount so as to mitigate issues of self-corrosion induced by photogenerated holes [5–7]. Despite the great effort devoted to developing photocatalysts embracing all these favorable attributes [8–10], the practical solar-to-hydrogen (STH) efficiency is still far from satisfactory, not to mention the formidability to balance

activity with stability, which has been always a dilemma in catalyst research [11,12]. To combat these obstacles, a viable solution is to combine heterogeneous photoabsorbers of high stability with redox-targeting co-catalysts of high activity, between which the band alignment and electronic coupling at the heterojunction are crucial to ensure a coherent charge and energy flow [13–15].

Defect engineering has been a widely reckoned tactic to simultaneously ameliorate all the above-mentioned attributes for a potent photocatalyst regarding light absorption, charge separation and redox conversion [16–18]. However, the role of the defects introduced remains controversial, as some claim they can serve as electron-trapping sites for improving the photogenerated charge separation [19,20], while others argue they would act as electron-hole recombination centers to shorten the lifetime and mean free path of photocarriers [21,22].

* Corresponding author at: Soochow Institute of Energy and Material Innovations, College of Energy, Jiangsu Key Laboratory for Advanced Carbon Materials and Wearable Energy Technologies, Soochow University, Suzhou 215006, China.

E-mail address: ypeng@suda.edu.cn (Y. Peng).

<https://doi.org/10.1016/j.apcatb.2023.122827>

Received 31 January 2023; Received in revised form 18 April 2023; Accepted 29 April 2023

Available online 30 April 2023

0926-3373/© 2023 Elsevier B.V. All rights reserved.

In such context, mechanistic understanding of the role of these structural and electronic defects in governing the charge and redox behaviors is pivotal to the development of high-performance photocatalyst for hydrogen production. Moreover, in heterogeneous photocatalytic systems engaging redox-targeting co-catalysts, the interplay between structural defects in the photoabsorber and active sites on the co-catalyst remains elusive and should be clarified for rational catalyst design.

Recently, Zinc indium sulfide (ZnIn_2S_4 , hereafter abbreviated as ZIS) with a layered structure has stood out among many promising photocatalysts for hydrogen production, mainly because of its high activity, good chemical stability, and appropriate bandgap (2.06–2.85 eV) corresponding to visible light absorption [23,24]. In general, a unit cell layer of ZIS comprises three sublayers, including a tetrahedral ZnS_4 surface layer, an octahedral InS_6 middle layer and another tetrahedral InS_4 bottom layer. Such a compositional and structural complexity of ZIS endows great opportunities to modulate its physicochemical properties [25,26]. Particularly, the photochemical properties of ZIS are largely dependent on its defect and surface states, which are tunable by introducing heteroatomic doping [27,28], cationic/anionic vacancies [29,30], as well as affixed heterostructures [31,32]. However, as aforementioned, the exact role of these introduced defect sites remains to be elucidated, calling for controllable and well-defined model catalytic systems. In all cases, the modification of ZIS chemical and electronic structure should be steered towards extending the separation and life time of photoexcited electron-hole pairs.

In the current study, we show the defect sites introduced into ZIS function as a double-bladed sword: on one hand, they act as recombination centers to impede photogenerated electron-hole separation in bulk ZIS; on the other hand, they drive electroless deposition and activation of the Pt co-catalyst through strong electronic coupling and thereby drastically enhance photocatalytic hydrogen production. The intimate coupling between the vacancy sites of ZIS and the deposited Pt

atoms/clusters not only promotes photoexcited electron-hole separation, but also modulates local charge polarization to leverage the intrinsic activity of the co-catalyst. As a result, the defective ZIS with a moderate Pt loading manifests the best hydrogen evolution rate of $15.56 \text{ mmol h}^{-1} \text{ g}^{-1}$ and a superb turn-over number of 99610 (92 h), which are among the best reported in literature. Comprehensive microscopic, spectroscopic and photoelectrochemical characterizations further testify that Pt atoms deposited at the defect sites reverse the adverse role the latter in bulk ZIS, turning them from exciton recombination centers to catalytic hot-spots.

2. Results and discussion

Two assemblies of flower-like ZnIn_2S_4 (ZIS) composed of clustered 2D nanosheets were prepared by the microwave-assisted and hydrothermal methods, and denoted as M-ZIS and H-ZIS, respectively (Fig. 1a, see Methods for synthetic details). Scanning electron microscope (SEM) images showed that M-ZIS exhibited a loosely packed "peony-like" morphology comprising thin and smooth petals of various sizes (Fig. 1b and c). In comparison, H-ZIS more resembled the looking of "hydrangea" with closely packed petals assembled in a spherical shape (Fig. 1f and g). Spherical aberration-corrected transmission electron microscope (AC-TEM) images revealed that M-ZIS had a defect-free lattice structure of long-range order (Fig. 1d, S1a), displaying nearly single crystallinity and the (102) crystal plane of ZnIn_2S_4 (Fig. 1e). In a stark contrast, H-ZIS manifested a polycrystalline nature with less-ordered lattice, containing enormous defects and grain boundaries (Fig. 1h, i and S1b). Energy-dispersive X-ray (EDX) elemental mapping images unveiled the uniform distribution of S, In, and Zn in both M-ZIS and H-ZIS without other impurities (Fig. S2). Taken together, the high-resolution microscopic observations above explicitly show that different synthetic protocols led to different morphology and microstructure of ZIS.

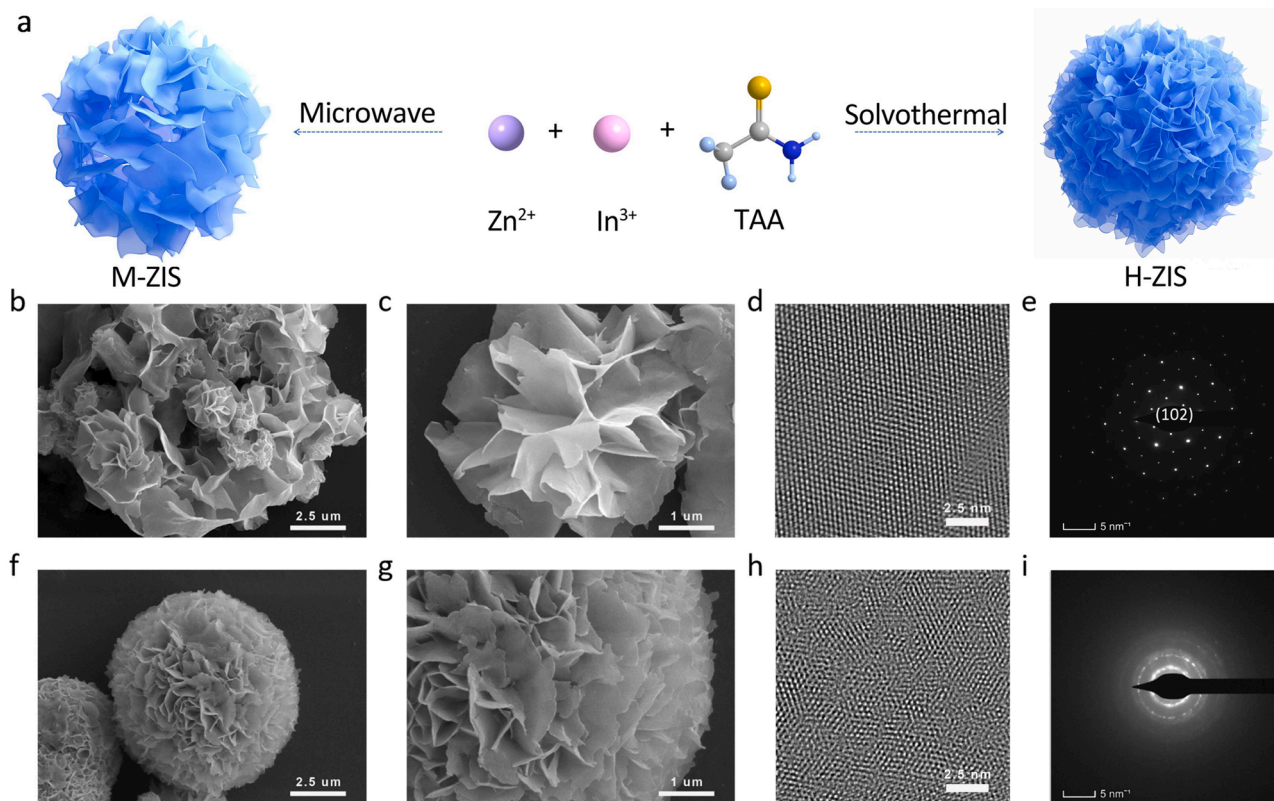


Fig. 1. Morphology and microstructure of ZnIn_2S_4 prepared by the microwave-assisted (M-ZIS) and hydrothermal (H-ZIS) methods. (a) Schematic illustration of the synthetic protocols and morphologies of M-ZIS and H-ZIS. (b, c) SEM of different magnification, (d) AC-TEM and (e) SAED pattern of M-ZIS. (f, g) SEM of different magnification, (h) AC-TEM and (i) SAED pattern of H-ZIS.

X-ray diffraction (XRD) spectrometry taken on M-ZIS and H-ZIS revealed similar diffraction patterns indexed to the $P\bar{3}m1$ group of hexagonal ZIS (JCPDS #65–2023, Fig. 2a). There were no other crystalline phases identified, confirming the good sample purity. Compared to M-ZIS, H-ZIS displayed a slight shift of diffraction peaks about 0.4° to smaller 2θ angles (Fig. S3), owing to its relatively disordered lattice structure with enriched defects and grain boundaries.[29] The defective nature of H-ZIS was further confirmed by electron spin resonance (ESR) measurements, revealing a strong ESR signal at $g = 2.006$ ascribed to the presence of S vacancies (Fig. 2b) [33]. By contrast, such ESR response was not observed for M-ZIS. X-ray photoelectron spectroscopy (XPS) survey spectra identified the coexistence of Zn, In, and S in both M-ZIS and H-ZIS (Fig. S4). In the high-resolution S 2p spectra (Fig. 2c), the S $2p_{3/2}$ and S $2p_{1/2}$ peaks of H-ZIS negatively shift about 0.12 eV and 0.14 eV, respectively, relative to those of M-ZIS. The negative shift of S 2p binding energies has been reportedly correlated to the generation of S vacancies in ZIS [34]. Both M-ZIS and H-ZIS displayed In 3d signals at the same binding energies, suggesting negligible difference in the electronic configuration of In 3d orbitals (Fig. S5). In contrast, the Zn 2p spin states of these two samples were significantly different, with both the Zn $2p_{3/2}$ and $2p_{1/2}$ peaks of H-ZIS shifted to lower binding energies, apart from a notably increased shoulder intensity (Fig. 2d). The increase in shoulder intensity might be attributed to the augmented shake-off excitation of the valence band [35], which will be explained later in more details. Collectively, these XPS observations corroborate the presence of S vacancies in H-ZIS, and suggest that the chemical state of Zn, rather than In, was mainly influenced by the change of S state. Obviously, to comply with the rule of charge neutrality the emergence of S vacancies would inevitably lower the oxidation state of Zn within the tetrahedral coordination sphere of $[\text{ZnS}_4]^{6-}$.

Raman spectra taken on M-ZIS and H-ZIS presented similar vibrational signals characteristic to those reported for ZIS (Fig. 2e) [36–38]. The three bands located at 243, 300, and 352 cm^{-1} are respectively

assigned to the LO_1 , TO_2 , and LO_2 modes of ZIS [37]. Note that the LO_1 mode in H-ZIS is apparently stronger than that in M-ZIS, inferring an enhancement in the longitudinal phonon mode at the $[\text{ZnS}_4]^{6-}$ tetrahedral sites due to the presence of S vacancies and symmetry loss [38]. BET analysis on N_2 adsorption/desorption isotherms revealed a slightly higher specific surface area of H-ZIS ($93\text{ m}^2\text{ g}^{-1}$ vs. $87\text{ m}^2\text{ g}^{-1}$ for M-ZIS) with enhanced meso-porosity (Fig. 2f, S6), which can be attributed to the more closely packed “hydrangea” morphology as seen in Fig. 1f and g.

To compare the optical properties of M-ZIS and H-ZIS, UV-Vis and Photoluminescence spectra were taken. Both ZIS samples displayed similar onset of UV-Vis absorption between 500 and 550 nm (Fig. S7). In the converted Tauc plots, the band gaps of M-ZIS and H-ZIS were respectively extrapolated at 2.54 and 2.57 eV, a very small difference (Fig. 3a). By contrast, a drastic difference in photoluminescence emission was observed for the two samples. The steady-state photoluminescence (ss-PL) spectra in Fig. 3b clearly show that M-ZIS displays a much lower PL intensity than H-ZIS does, in virtue of the alleviated recombination of excitons. Furthermore, the time-resolved photoluminescence (tr-PL) spectra in Fig. 3c unravel a longer average exciton lifetime of 0.86 ns for M-ZIS (vs. 0.44 ns for H-ZIS, see Methods for fitting and calculation details). Both the intensified quench and extended relaxation of photoluminescence emission on M-ZIS are in line with the common view that semiconductors with ordered lattice and minimal defects are favorable to extend the mean free path and lifetime of charge carriers, which are in turn beneficial to the efficient separation of photogenerated electron-hole pairs.

Ultraviolet Photoelectron Spectroscopy was used to estimate the band structure of M-ZIS and H-ZIS. On one side, the work functions of M-ZIS and H-ZIS quantified by the cut-off binding energies were determined to be 4.28 and 3.77 eV (relative to the vacuum level), respectively (Fig. 3d, left panel). This indicates that the photoelectrons are easier to escape from the defective lattice of the latter, and also explains the

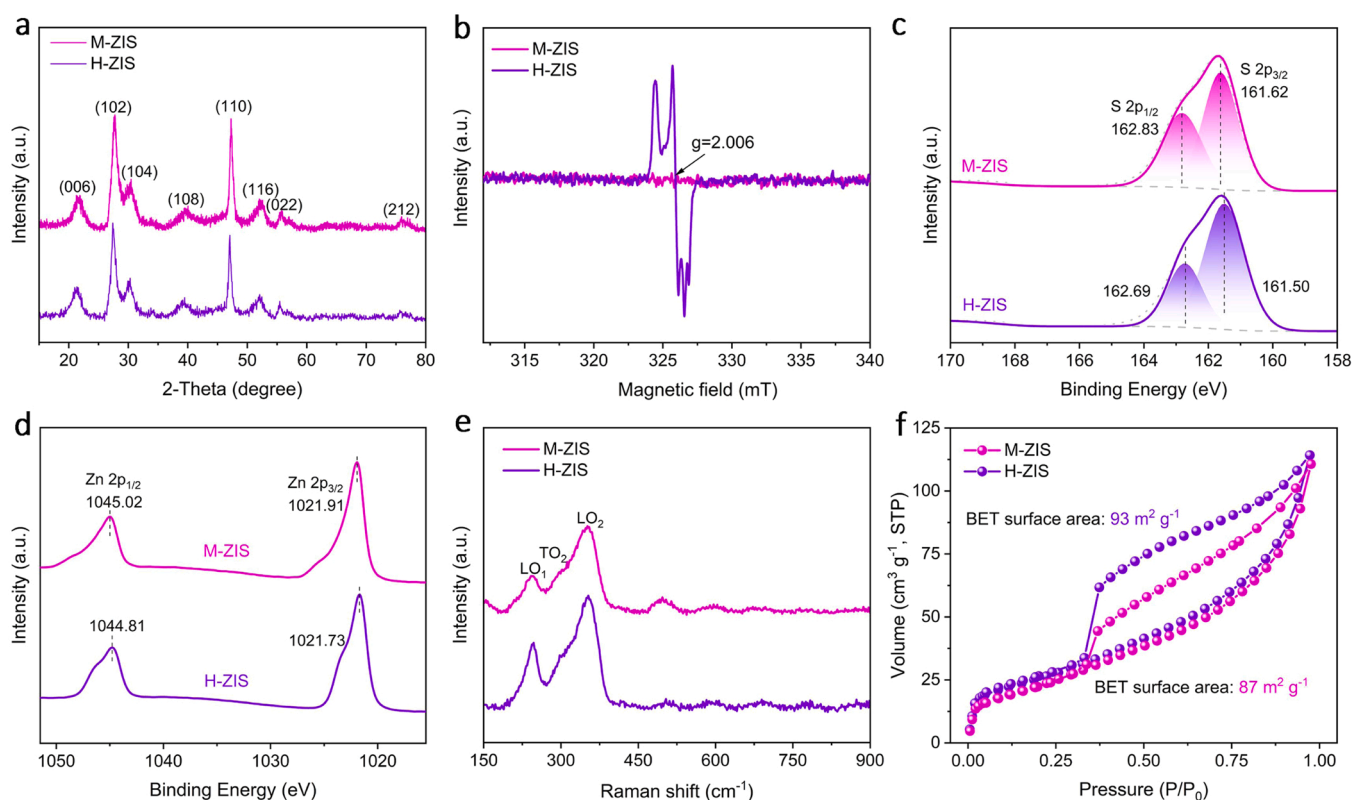


Fig. 2. Physicochemical properties of M-ZIS and H-ZIS. (a) XRD patterns, (b) ESR spectra, (c) XPS S 2p and (d) Zn 2p spectra, (e) Raman spectra, and (f) Nitrogen adsorption-desorption isotherms.

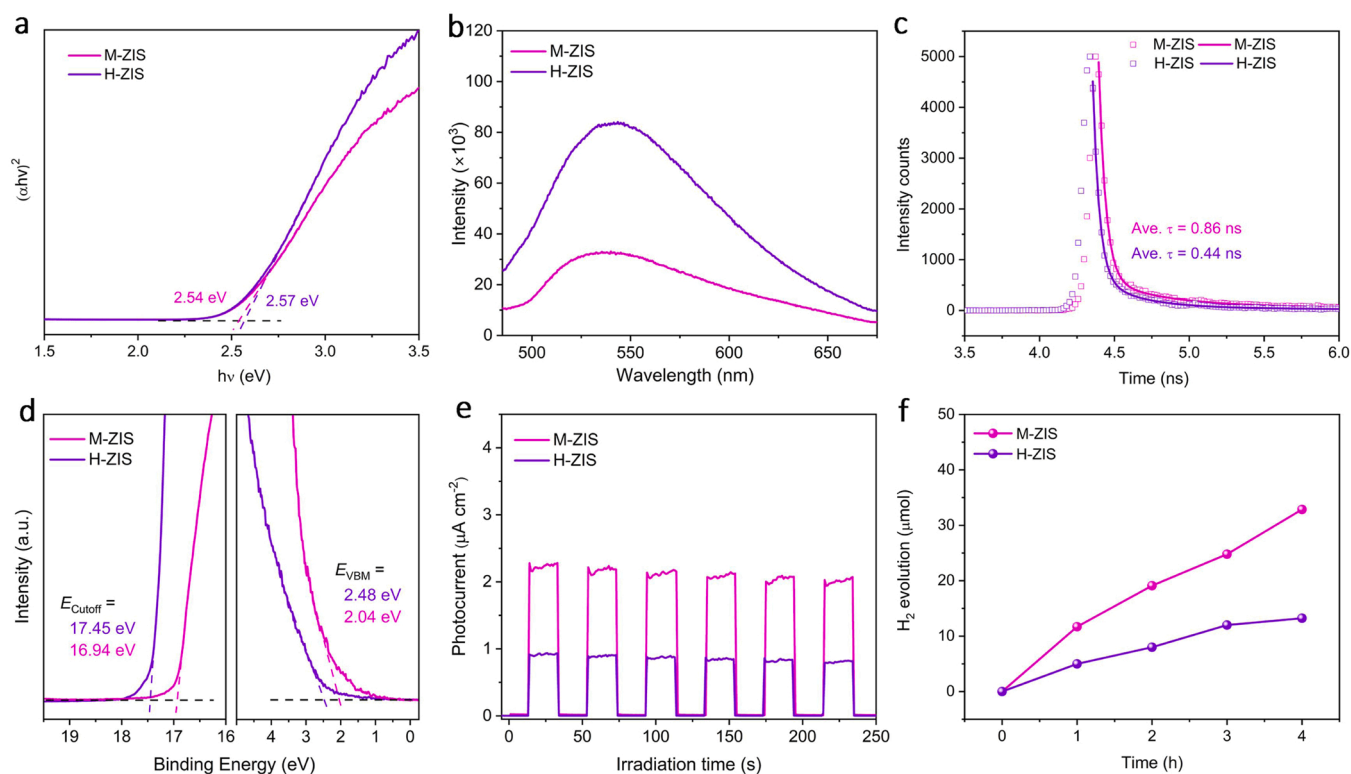


Fig. 3. Photochemical properties of M-ZIS and H-ZIS. (a) Tauc plots converted from the UV-Vis DRS spectra, (b) Steady-state PL spectra, (c) Time-resolved PL decay spectra, (d) UPS spectra, (e) Transient photocurrent response in 0.2 M Na₂SO₄ aqueous solution and (f) photocatalytic H₂ yield under simulated sunlight with an AM 1.5 G filter.

intensified shake-off shoulder as seen in the XPS Zn 2p spectrum (Fig. 2d). On the other side, the valence band maximum (VBM) of M-ZIS and H-ZIS were found located at 2.04 and 2.48 eV below the Fermi level, respectively (Fig. 3d, right panel). In conjunction with the band gaps obtained from the Tauc plots, the band structures of M-ZIS and H-ZIS comprising the conduction band minimum (CBM), the Fermi level inside the band gap, and the VBM can be derived as shown in Fig. S8. Note that the two samples exhibit similar energy levels of CBM and VBM, but the Fermi level of H-ZIS is closer to CBM, suggesting it possesses more n-type characteristics. This can be well understood from the defective nature of H-ZIS containing more S vacancies and free electrons, which is in line with the ESR and XPS results.

The photochemical properties of M-ZIS and H-ZIS were further compared by transient photocurrent response (TPR) under intermittent irradiation (Fig. 3e) and photocatalytic hydrogen evolution reaction (Fig. 3f). The TPR *i-t* plots show that M-ZIS exhibits a much higher photocurrent than that of H-ZIS (Fig. 3e), evidencing its better charge separation upon light excitation. When applied as photocatalysts to drive water splitting for hydrogen production (under visible light with triethanolamine (TEOA) serving as the hole scavenger), M-ZIS yielded a total of 32.9 μmol H₂ within the 4-hour testing period (Fig. 3f), which was 2.5 folds of that produced by H-ZIS (13.2 μmol). Taken together from the structural and photochemical characterizations above, we are able to conclude that M-ZIS with more ordered lattice and less structural defects manifests a better photocarrier separation and thereby a better photocatalytic performance, provided that there were no co-catalysts engaged.

To further raise the performance bars of M-ZIS and H-ZIS in photocatalytic hydrogen production, elemental Pt as the co-catalyst was deposited onto the surface of these photoabsorbers. In the electroless photo-deposition process, the amount of Pt deposition was regulated by the volume of K₂PtCl₆ solution added to the ZIS dispersion (see Methods for preparation details). Of note, Pt was found more readily deposited

onto the surface of H-ZIS than on M-ZIS. Comparatively, adding 10, 20, 40, and 100 μL of the K₂PtCl₆ solution (5 mg mL⁻¹) respectively resulted in the actual Pt deposition of 0.13%, 0.21%, 0.35%, and 0.51% (in weight percentage) on H-ZIS, whereas adding the same amount of K₂PtCl₆ yielded the Pt weight ratio of 0.08%, 0.11%, 0.19%, and 0.26% on M-ZIS. In general, the amount of Pt deposition on all samples were small (all less than 1%), and under the same condition Pt deposited on H-ZIS was roughly twice of that on M-ZIS (Table S2). These observations strongly suggest that the defect sites on H-ZIS facilitates Pt deposition.

In the subsequent tests on photocatalytic hydrogen production (Table S3), the sample of H-ZIS with a Pt loading of 0.13% (denoted as H-ZIS/Pt_{0.13} hereafter) produced the highest hydrogen yield of 311.1 μmol within 4 h, which is 23.6 and 1.2 folds higher than the H₂ yields of pristine H-ZIS and H-ZIS/Pt_{0.08}, respectively (Fig. 4a, S9). No changes of sample morphology and crystalline structure were observed on H-ZIS/Pt_{0.13} after the 4-hour test (Fig. S10). Further increasing the Pt loading on H-ZIS led to the decrease in hydrogen production (Fig. 4b, S9). On the other hand, the hydrogen production by Pt-loaded M-ZIS increased continuously with the increasing Pt loading, albeit in a gradual fashion. With the similar Pt content to that of H-ZIS/Pt_{0.13}, M-ZIS/Pt_{0.11} and M-ZIS/Pt_{0.19} only yielded a total hydrogen production of 75.6 and 85.4 μmol, respectively, in 4 h (Fig. S9). Thus, it is obvious that the Pt co-catalyst initially deposited on H-ZIS possesses a much higher activity than that on M-ZIS (Fig. 4c), and therefore led to a performance reversal in contrast to their pristine forms (Fig. 4a, b). However, when excess amount of Pt was deposited onto H-ZIS as in the case of H-ZIS/Pt_{0.51}, the hydrogen production (90.7 μmol in 4 h) is even inferior to that of M-ZIS/Pt_{0.26} (99.9 μmol in 4 h). This comparison, in conjunction with the decreasing trend of H₂ production at higher Pt loading observed for H-ZIS, implies that the early deposited Pt on H-ZIS is particularly active and such activity decays with the increasing Pt loading due to particle agglomeration (Fig. S11). It further infers that only the Pt atoms strongly coupled to the defective surface are highly active, which will be

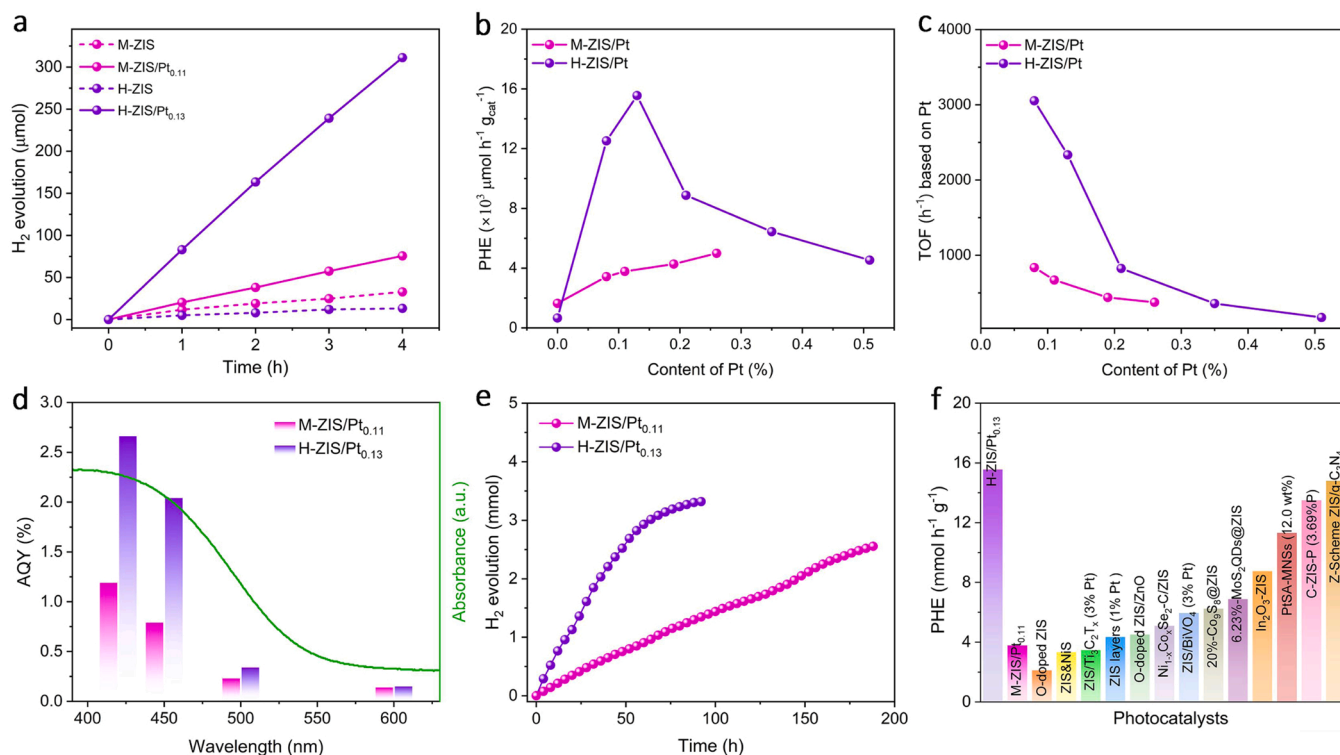


Fig. 4. Photocatalytic properties of M-ZIS/Pt_{0.11} and H-ZIS/Pt_{0.13}. (a) Comparison of photocatalytic H₂ evolution within 4 h for M-ZIS, H-ZIS, M-ZIS/Pt_{0.11} and H-ZIS/Pt_{0.13}. (b) Photocatalytic H₂ evolution normalized to the catalyst weight for M-ZIS and H-ZIS with various Pt loadings. (c) TOF normalized to Pt loading for M-ZIS and H-ZIS with various Pt contents. (d) Wavelength-dependent AQY measured for M-ZIS/Pt_{0.11} and H-ZIS/Pt_{0.13} at 420, 450, 500 and 600 nm (the green curve is the absorption spectra of M-ZIS). (e) Stability tests on the continuous hydrogen evolution catalyzed by H-ZIS/Pt_{0.13} and M-ZIS/Pt_{0.11}. (f) Comparison of PHE from this study with those of state-of-the-art chalcogenide catalysts reported in literature (see Table S5† for reference details).

interrogated later in more details.

A series of control experiments were conducted by varying the experimental parameters to validate the photocatalytic role of H-ZIS/Pt_{0.13} (Table S3, Entries 12–14), which is the best among all samples investigated in this study with regard to the rate of photocatalytic hydrogen evolution (PHE, Fig. 4b). In the absence of photocatalyst or light irradiation, there were no gaseous products detected during the 4-hour reaction period, confirming that the reaction is indeed photocatalytically driven (Fig. S12). When TEOA was not added, H-ZIS/Pt_{0.13} alone produced only 7.7 μmol H₂ in 4 h, verifying that under the experimental condition of this study TEOA plays an indispensable role as the hole scavenger. Both H-ZIS/Pt_{0.13} and M-ZIS/Pt_{0.11} exhibited a wavelength-dependent catalytic activity, with the maximal AQY of 2.66% and 1.19% attained at 420 nm light irradiation, respectively (Fig. 4d, Table S4). Note that the AQY-wavelength profiles of both samples are in consistency with the UV-Vis absorption of ZIS. Moreover, both H-ZIS/Pt_{0.13} and M-ZIS/Pt_{0.11} manifested outstanding photocatalytic stability, with the former producing 3319 μmol H₂ in a total of 92 h and the latter producing 2554.5 μmol H₂ in 188 h (Fig. 4e). Accordingly, the turnover number (TON) of H-ZIS/Pt_{0.13} reached to 99610 and that of M-ZIS/Pt_{0.11} reached to 90605. The PHE rate, turnover frequency (TOF) and TON of H-ZIS/Pt_{0.13} far exceeds those reported for heterogeneous photocatalysts based on ZIS and other metal sulfides (Fig. 4f, Table S5). Nonetheless, it should be noted that although the PHE rate of H-ZIS/Pt_{0.13} was much higher than that of M-ZIS/Pt_{0.11}, it reached a plateau of H₂ yield after about 90 h of operation. This observation collaterally infers that the higher activity of active sites on H-ZIS/Pt_{0.13} is accompanied by earlier photo-corrosion, especially on the S-vacancy sites.

To gain insights into the higher photocatalytic activity observed on H-ZIS/Pt_{0.13}, high-angle annular dark-field scanning transmission electron microscopy (HAADF-STEM) was carried out to visualize the Pt

deposition on both H-ZIS/Pt_{0.13} and M-ZIS/Pt_{0.11}. Typically, elements with higher atomic number exhibit a brighter contrast in the HAADF-STEM image. As shown by the high-resolution atomistic image in Fig. 5a, the distribution of Pt is not homogeneous on the nanosheet surface of H-ZIS/Pt_{0.13}, forming aggregated patches of sub- to a few nanometers. In contrast, the Pt distribution on M-ZIS/Pt_{0.11} is more uniform without obvious clustering (Fig. 5b). At larger scale, EDX-mapping images revealed the even distribution of Zn, In S and Pt on both samples (Fig. S13 and S14). XRD patterns showed that the crystalline phases of both H-ZIS/Pt_{0.13} and M-ZIS/Pt_{0.11} were unchanged after Pt deposition without discernible peak shift and any Pt-related diffraction peaks (Fig. 5c). This indicates that Pt atoms deposited on both samples were poorly crystallized, which is consistent with the above TEM observations. After Pt deposition, the strong ESR signal initially observed on H-ZIS was mostly vanished (Fig. 5d), likely due to the interplay between Pt and S vacancies to dissipate unpaired electrons. [39] Meanwhile, the ESR signal on M-ZIS/Pt_{0.11} remained indistinguishable. While the Raman peaks of M-ZIS/Pt_{0.11} remain unchanged when compared to M-ZIS, the LO₁ mode on H-ZIS/Pt_{0.13} vanished completely (Fig. 5e). Again, this indicates the interruption of the longitudinal phonon mode at the defective [ZnS₄]⁶⁻ tetrahedral sites by Pt deposition. [38] Taken together, these microscopic and spectroscopic evidences jointly support the strong coupling between the deposited Pt and substrate defects on H-ZIS/Pt_{0.13}.

XPS was further employed to probe the change of chemical states on both H-ZIS and M-ZIS after Pt deposition. The high-resolution Pt 4f spectra showed that the peaks of Pt on H-ZIS/Pt_{0.13}, in comparison to those of M-ZIS/Pt_{0.11}, shifted obviously to lower binding energies, corroborating a strong coupling between Pt and the H-ZIS substrate (Fig. 5f). Due to the defect-driven Pt deposition, the exterior orbitals of Pt receive electron donation from the surrounding S atoms, resulting in a negative shift of binding energies. Correspondingly, the S 2p signals of

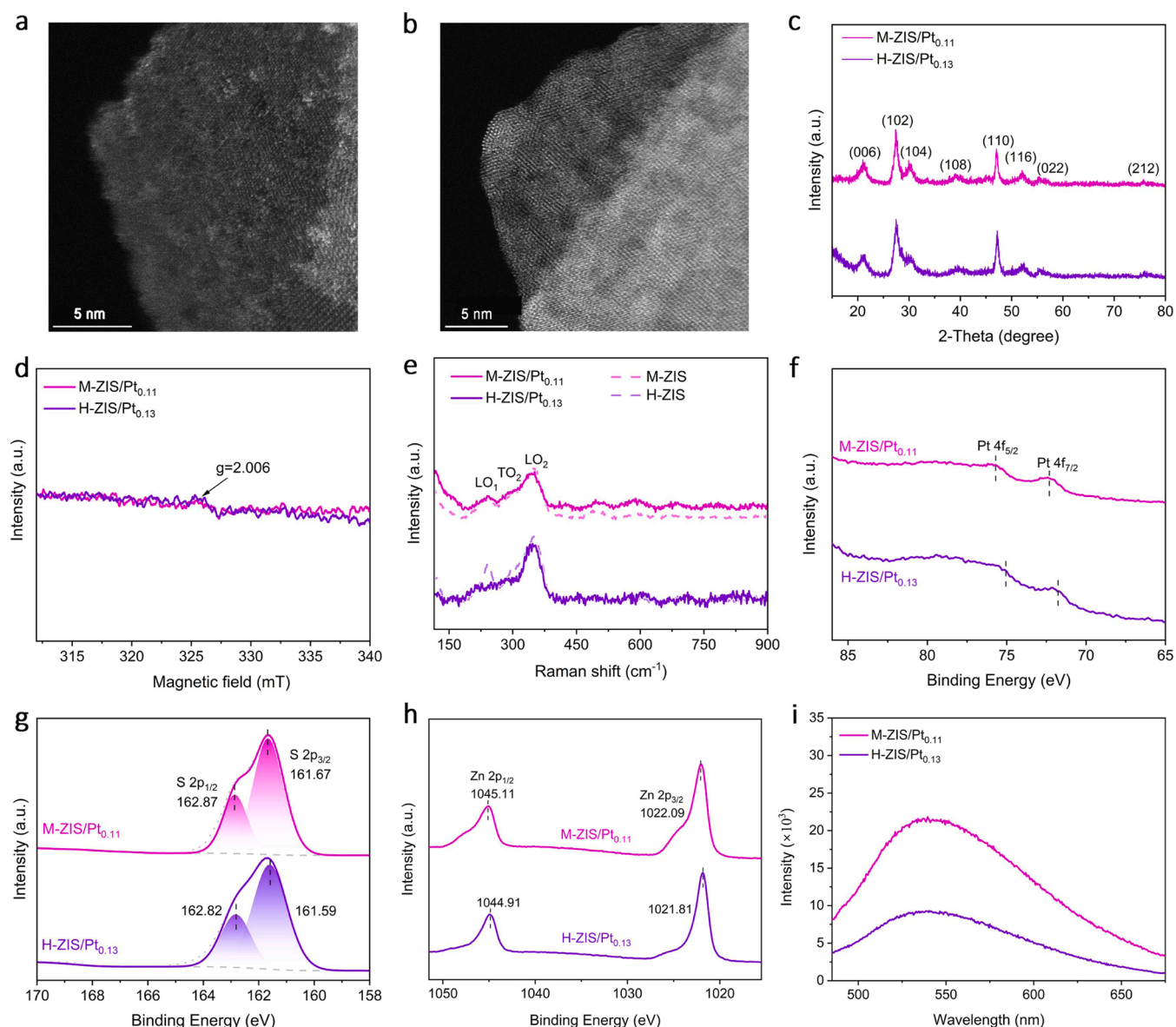


Fig. 5. Mechanistic investigations into the high photocatalytic activity of H-ZIS/Pt_{0.13} through structural characterizations. AC-TEM images of (a) H-ZIS/Pt_{0.13} and (b) M-ZIS/Pt_{0.11} in the HAADF-STEM mode. (c) XRD patterns, (d) ESR spectra and (e) Raman spectra of M-ZIS/Pt_{0.11} and H-ZIS/Pt_{0.13}. High-resolution XPS spectra of (f) Pt 4f, (g) S 2p, and (h) Zn 2p in M-ZIS/Pt_{0.11} and H-ZIS/Pt_{0.13}. (i) Steady-state PL spectra of M-ZIS/Pt_{0.11} and H-ZIS/Pt_{0.13}.

H-ZIS/Pt_{0.13} shifted positively by about 0.1 eV, whereas those of M-ZIS/Pt_{0.11} remained mostly unchanged before and after Pt deposition (Fig. 5g vs 2c). A more eminent change of Zn chemical state was observed on H-ZIS/Pt_{0.13} after Pt deposition (Fig. 5h vs 2d). Not only the binding energy of Zn 2p_{1/2} and 2p_{3/2} shifted to higher values, but also their shoulder peaks weakened significantly. As aforementioned, the change of Zn²⁺ shoulder intensity might result from the change of work function due to Pt deposition.[35] Meanwhile, the chemical states of In³⁺ kept about the same for all samples including H-ZIS and M-ZIS before and after Pt deposition (Fig. S15 vs S5), corroborating that the In element is chemically inert in all sample treatments of this study. This provides extra evidence for the interaction of Pt with S vacancies in the [ZnS₄]⁶⁻ coordination sphere. As such, the defective H-ZIS substrate with higher surface energy binds more strongly to the Pt atoms and therefore promotes the electron transfer from the photoabsorber to the co-catalyst upon photoexcitation, which was indeed witnessed by the reversed intensity of ss-PL emission as shown in Fig. 5i (vs. Fig. 3b).

Lastly, the mechanism of M-ZIS and H-ZIS to drive photocatalytic hydrogen production with and without the aid of Pt co-catalyst is

summarized in Fig. 6. M-ZIS nanosheets prepared by the microwave method possess a consummate lattice with less defects, lending improved charge separation and transport efficiency upon light excitation (Fig. 6a). In comparison, H-ZIS nanosheets prepared by the hydrothermal method manifest markedly disordered lattice with enriched S vacancies, accelerating the electron-hole recombination during the photocatalytic process (Fig. 6b). When elemental Pt as the co-catalyst is deposited onto the surface of these two photoabsorbers, the activity trend is reversed. Pt is more readily deposited onto H-ZIS than M-ZIS due to the existence of surface defects, forming small clusters at the defect sites (Fig. 6c vs 6d). The enhanced electronic coupling between surface defects and Pt turns them into catalytically “hot spots” to achieve a remarkable photocatalytic hydrogen performance. We also note that the high activity of the small Pt clusters interacted with surface defects can be offset by their larger particle size.

3. Conclusions

In summary, two types of ZIS photoabsorbers of different

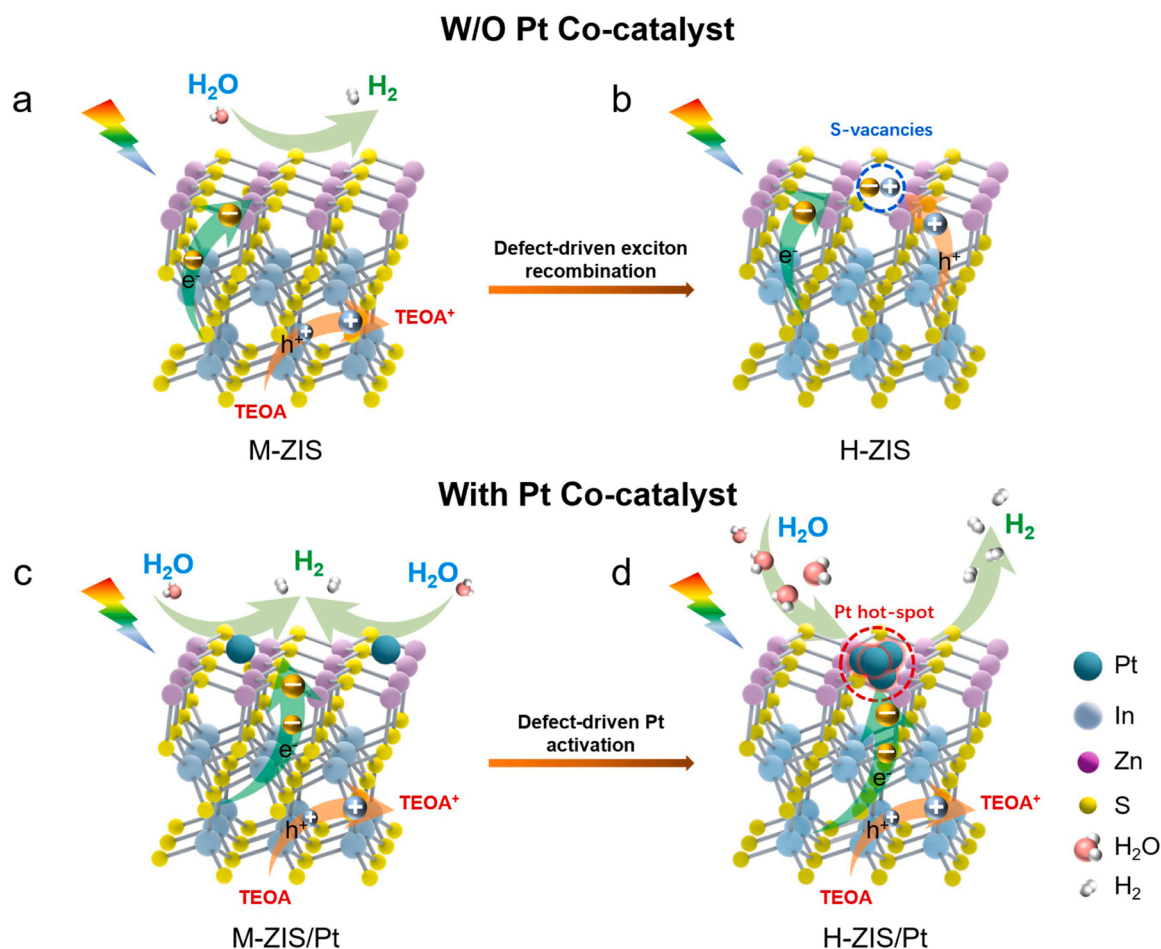


Fig. 6. Schematic illustration of (a) M-ZIS possessing a consummate lattice with few defects, (b) defect-induced photocarrier recombination in H-ZIS, (c) M-ZIS/Pt with a weak coupling between ZIS and Pt, and (d) the defect-driven Pt activation on H-ZIS/Pt.

crystallinity were successfully prepared via different synthetic protocols. When no co-catalyst was involved, M-ZIS yielded a total of 32.9 μmol H_2 within the 4-hour testing period, which was 2.5 folds of that produced by H-ZIS (13.2 μmol). This indicates that the more ordered lattice of M-ZIS with less structural defects affords a better photocarrier separation and thereby endows a better photocatalytic performance. Surprisingly, the activity trend of photochemical reaction was completely reversed when Pt was deposited as the co-catalyst. The best photocatalysts of H-ZIS/Pt_{0.13} produced 311.1 μmol H_2 in 4 h, accounting for a Pt-based TOF of 2334 h^{-1} , which are significantly higher than the values of M-ZIS/Pt_{0.11} (75.6 μmol in 4 h, TOF = 670 h^{-1}) with similar amount of Pt deposition. More remarkably, H-ZIS/Pt_{0.13} demonstrated a high TON of 99610 in a total of 92 h, which is among the best of chalcogenide-based photocatalysts reported in literature. Through comprehensive microscopic and spectroscopic characterizations, the enhanced photocatalytic performance observed on Pt-deposited H-ZIS sheets was attributed to the enhanced electronic coupling between the photoabsorber and co-catalyst, in virtue of the defect-driven electroless deposition and activation of Pt atoms. Our next efforts would be to take advantage of the band structure of ZIS spanning across both the HER and OER equilibrium potentials (Fig. S8) to realize overall water splitting by consecutively depositing OER co-catalyst on the nanosheet surface.

CRediT authorship contribution statement

Yanhui Su: Writing – original draft, Validation, Formal analysis, Visualization, Software, Methodology. **Zhihe Wei:** Visualization, Investigation. **Yuebin Lian:** Schematic drawing. **Qiaoqiao Mu, Weiye**

Pan and Daqi Song: Raman and SEM data collection. **Yongze Qin, Wei Hua and Jian Cheng:** BET and infrared data collection, logical reasoning. **Zhao Deng:** Data curation. **Yang Peng:** Writing – review & editing have approved the manuscript and agree with this submission.

Declaration of Competing Interest

The authors declare that they have no known competing financial interests or personal relationships that could have appeared to influence the work reported in this paper.

Data Availability

Data will be made available on request.

Acknowledgements

This work was financially supported by National Natural Science Foundation of China (No. 22072101, 22075193), Natural Science Foundation of Jiangsu Province (No. BK20221239, BK20211306), Six Talent Peaks Project in Jiangsu Province (No. TD-XCL-006) and Priority Academic Program Development (PAPD) of Jiangsu Higher Education Institutions.

Appendix A. Supporting information

Supplementary data associated with this article can be found in the online version at [doi:10.1016/j.apcatb.2023.122827](https://doi.org/10.1016/j.apcatb.2023.122827).

References

- [1] M. Torras, P. Molet, L. Soler, J. Llorca, A. Roig, A. Mihi, Au/TiO₂ 2D-photonic crystals as UV-visible photocatalysts for H₂ production, *Adv. Energy Mater.* 12 (2021) 2103733.
- [2] T. Kawawaki, Y. Mori, K. Wakamatsu, S. Ozaki, M. Kawachi, S. Hossain, Y. Negishi, Controlled colloidal metal nanoparticles and nanoclusters: recent applications as cocatalysts for improving photocatalytic water-splitting activity, *J. Mater. Chem. A* 8 (2020) 16081–16113.
- [3] F. Zhao, N. Zhang, H. Li, X. Zhang, Z. Luo, Y. Wang, Photocatalyst with chloroplast-like structure for enhancing hydrogen evolution reaction, *Energy Environ. Mater.* 0 (2021) 1–9.
- [4] W. Wang, Y. Tao, J. Fan, Z. Yan, H. Shang, D.L. Phillips, M. Chen, G. Li, Fullerene-graphene acceptor drives ultrafast carrier dynamics for sustainable CdS photocatalytic hydrogen evolution, *Adv. Funct. Mater.* 32 (2022) 2201357.
- [5] C.Q. Li, X. Du, S. Jiang, Y. Liu, Z.L. Niu, Z.Y. Liu, S.S. Yi, X.Z. Yue, Constructing direct Z-scheme heterostructure by enwrapping ZnIn₂S₄ on CdS hollow cube for efficient photocatalytic H₂ generation, *Adv. Sci.* 9 (2022), e2201773.
- [6] W. Li, F. Wang, X.-y. Liu, Y.-y. Dang, J.-y. Li, T.-h. Ma, C.-y. Wang, Promoting body carriers migration of CdS nanocatalyst by N-doping for improved hydrogen production under simulated sunlight irradiation, *Appl. Catal. B: Environ.* 313 (2022), 121470.
- [7] Q. Mu, Y. Su, Z. Wei, H. Sun, Y. Lian, Y. Dong, P. Qi, Z. Deng, Y. Peng, Dissecting the interfaces of MOF-coated CdS on synergized charge transfer for enhanced photocatalytic CO₂ reduction, *J. Catal.* 397 (2021) 128–136.
- [8] Y. Li, L. Yang, H. He, L. Sun, H. Wang, X. Fang, Y. Zhao, D. Zheng, Y. Qi, Z. Li, W. Deng, In situ photodeposition of platinum clusters on a covalent organic framework for photocatalytic hydrogen production, *Nat. Commun.* 13 (2022) 1355.
- [9] A. Kumar Singh, C. Das, A. Indra, Scope and prospect of transition metal-based cocatalysts for visible light-driven photocatalytic hydrogen evolution with graphitic carbon nitride, *Coord. Chem. Rev.* 465 (2022), 214516.
- [10] Y. Guo, Q. Zhou, J. Nan, W. Shi, F. Cui, Y. Zhu, Perylenetetracarboxylic acid nanosheets with internal electric fields and anisotropic charge migration for photocatalytic hydrogen evolution, *Nat. Commun.* 13 (2022) 2067.
- [11] M. Rahman, H. Tian, T. Edvinsson, Revisiting the limiting factors for overall water-splitting on organic photocatalysts, *Angew. Chem. Int. Ed. Engl.* 59 (2020) 16278–16293.
- [12] S. Wang, L. Wang, W. Huang, Bismuth-based photocatalysts for solar energy conversion, *J. Mater. Chem. A* 8 (2020) 24307–24352.
- [13] S. Chen, J.J.M. Vequizo, Z. Pan, T. Hisatomi, M. Nakabayashi, L. Lin, Z. Wang, K. Kato, A. Yamakata, N. Shibata, T. Takata, T. Yamada, K. Domen, Surface modifications of (ZnSe)_{0.5}(CuGa_{2.5}Se_{4.25})_{0.5} to promote photocatalytic Z-scheme overall water splitting, *J. Am. Chem. Soc.* 143 (2021) 10633–10641.
- [14] M. Tan, Y. Ma, C. Yu, Q. Luan, J. Li, C. Liu, W. Dong, Y. Su, L. Qiao, L. Gao, Q. Lu, Y. Bai, Boosting photocatalytic hydrogen production via interfacial engineering on 2D ultrathin Z-scheme ZnIn₂S₄/g-C₃N₄ heterojunction, *Adv. Funct. Mater.* (2021) 2111740.
- [15] Y. Su, Z. Song, W. Zhu, Q. Mu, X. Yuan, Y. Lian, H. Cheng, Z. Deng, M. Chen, W. Yin, Y. Peng, Visible-light photocatalytic CO₂ reduction using metal-organic framework derived Ni(OH)₂ nanocages: a synergy from multiple light reflection, static charge transfer, and oxygen vacancies, *ACS Catal.* (2020) 345–354.
- [16] L. Ran, J. Hou, S. Cao, Z. Li, Y. Zhang, Y. Wu, B. Zhang, P. Zhai, L. Sun, Defect engineering of photocatalysts for solar energy conversion, *Sol. RRL* 4 (2020) 1900487.
- [17] J. Xiong, J. Di, J. Xia, W. Zhu, H. Li, Surface defect engineering in 2D nanomaterials for photocatalysis, *Adv. Funct. Mater.* 28 (2018) 1801983.
- [18] J. Zhou, J. Zhao, R. Liu, Defect engineering of zeolite imidazole framework derived ZnS nanosheets towards enhanced visible light driven photocatalytic hydrogen production, *Appl. Catal. B: Environ.* 278 (2020), 119265.
- [19] S. Bai, N. Zhang, C. Gao, Y. Xiong, Defect engineering in photocatalytic materials, *Nano Energy* 53 (2018) 296–336.
- [20] D. Maarisetty, S. Mahanta, A.K. Sahoo, P. Mohapatra, S.S. Baral, Steering the charge kinetics in dual-functional photocatalysis by surface dipole moments and band edge modulation: a defect study in TiO₂-ZnS-rGO composites, *ACS Appl. Mater. Interfaces* 12 (2020) 11679–11692.
- [21] S. Zhang, Y. Si, B. Li, L. Yang, W. Dai, S. Luo, Atomic-level and modulated interfaces of photocatalyst heterostructure constructed by external defect-induced strategy: a critical review, *Small* 17 (2021), e2004980.
- [22] Y. Zhang, Y. Li, H. Yu, K. Yu, H. Yu, Interfacial defective Ti³⁺ on Ti/TiO₂ as visible-light responsive sites with promoted charge transfer and photocatalytic performance, *J. Mater. Sci. Technol.* 106 (2022) 139–146.
- [23] Q. Luan, X. Xue, R. Li, L. Gu, W. Dong, D. Zhou, X. Wang, B. Li, G. Wang, C. Hou, Boosting photocatalytic hydrogen evolution: Orbital redistribution of ultrathin ZnIn₂S₄ nanosheets via atomic defects, *Appl. Catal. B: Environ.* 305 (2022), 121007.
- [24] X. Zheng, Y. Song, Y. Liu, Y. Yang, D. Wu, Y. Yang, S. Feng, J. Li, W. Liu, Y. Shen, X. Tian, ZnIn₂S₄-based photocatalysts for photocatalytic hydrogen evolution via water splitting, *Coord. Chem. Rev.* 475 (2023), 214898.
- [25] J. Wan, L. Liu, Y. Wu, J. Song, J. Liu, R. Song, J. Low, X. Chen, J. Wang, F. Fu, Y. Xiong, Exploring the polarization photocatalysis of ZnIn₂S₄ material toward hydrogen evolution by integrating cascade electric fields with hole transfer vehicle, *Adv. Funct. Mater.* 32 (2022) 2203252.
- [26] S. Zhang, X. Liu, C. Liu, S. Luo, L. Wang, T. Cai, Y. Zeng, J. Yuan, W. Dong, Y. Pei, Y. Liu, MoS₂ Quantum dot growth induced by S vacancies in a ZnIn₂S₄ monolayer: atomic-level heterostructure for photocatalytic hydrogen production, *ACS Nano* 12 (2018) 751–758.
- [27] C. Du, B. Yan, Z. Lin, G. Yang, Enhanced carrier separation and increased electron density in 2D heavily N-doped ZnIn₂S₄ for photocatalytic hydrogen production, *J. Mater. Chem. A* 8 (2020) 207–217.
- [28] W. Yang, L. Zhang, J. Xie, X. Zhang, Q. Liu, T. Yao, S. Wei, Q. Zhang, Y. Xie, Enhanced photoexcited carrier separation in oxygen-doped ZnIn₂S₄ nanosheets for hydrogen evolution, *Angew. Chem. Int. Ed. Engl.* 55 (2016) 6716–6720.
- [29] W. Xu, W. Gao, L. Meng, W. Tian, L. Li, Incorporation of sulfate anions and sulfur vacancies in ZnIn₂S₄ photoanode for enhanced photoelectrochemical water splitting, *Adv. Energy Mater.* 11 (2021) 2101181.
- [30] Y. He, C. Chen, Y. Liu, Y. Yang, C. Li, Z. Shi, Y. Han, S. Feng, Quantitative evaluation of carrier dynamics in full-spectrum responsive metallic ZnIn₂S₄ with indium vacancies for boosting photocatalytic CO₂ reduction, *Nano Lett.* 22 (2022) 4970–4978.
- [31] M.Q. Yang, Y.J. Xu, W. Lu, K. Zeng, H. Zhu, Q.H. Xu, G.W. Ho, Self-surface charge exfoliation and electrostatically coordinated 2D hetero-layered hybrids, *Nat. Commun.* 8 (2017) 14224.
- [32] J. Hu, C. Chen, Y. Zheng, G. Zhang, C. Guo, C.M. Li, Spatially separating redox centers on Z-scheme ZnIn₂S₄/BiVO₄ hierarchical heterostructure for highly efficient photocatalytic hydrogen evolution, *Small* 16 (2020), e2002988.
- [33] X. Wang, X. Wang, J. Huang, S. Li, A. Meng, Z. Li, Interfacial chemical bond and internal electric field modulated Z-scheme S_v-ZnIn₂S₄/MoSe₂ photocatalyst for efficient hydrogen evolution, *Nat. Commun.* 12 (2021) 4112.
- [34] C. Du, Q. Zhang, Z. Lin, B. Yan, C. Xia, G. Yang, Half-unit-cell ZnIn₂S₄ monolayer with sulfur vacancies for photocatalytic hydrogen evolution, *Appl. Catal. B: Environ.* 248 (2019) 193–201.
- [35] D. Cabrera-German, G. Molar-Velázquez, G. Gómez-Sosa, W. de la Cruz, A. Herrera-Gomez, Detailed peak fitting analysis of the Zn 2p photoemission spectrum for metallic films and its initial oxidation stages, *Surf. Interface Anal.* 49 (2017) 1078–1087.
- [36] S. Shen, L. Zhao, X. Guan, L. Guo, Improving visible-light photocatalytic activity for hydrogen evolution over ZnIn₂S₄: A case study of alkaline-earth metal doping, *J. Phys. Chem. Solids* 73 (2012) 79–83.
- [37] S. Shen, L. Zhao, L. Guo, Morphology, structure and photocatalytic performance of ZnIn₂S₄ synthesized via a solvothermal/hydrothermal route in different solvents, *J. Phys. Chem. Solids* 69 (2008) 2426–2432.
- [38] S.A. Lopez-Rivera, L. Martinez, B. Fontal, W. Giriat, F. Medina, Raman study of a ZnIn₂S₄ layered compound, *Semicond. Sci. Technol.* 10 (1995) 645–652.
- [39] X. Shi, C. Dai, X. Wang, J. Hu, J. Zhang, L. Zheng, L. Mao, H. Zheng, M. Zhu, Protruding Pt single-sites on hexagonal ZnIn₂S₄ to accelerate photocatalytic hydrogen evolution, *Nat. Commun.* 13 (2022) 1287.